Reversible dual stimuli-responsive polymer coatings with antimicrobial properties for oil–water separation

Nong Wang [a*], Haoqian Wang [a], Ke Wang [a], Jiajun Zuo [a], Zhihang Wang [b, c*]

[a] *School of Chemistry and Chemical Engineering, Lanzhou Jiaotong University, Lanzhou 730070, China*

[b] *School of Engineering, College of Science and Engineering, University of Derby, Markeaton Street, Derby DE2 23AW, United Kingdom*

[c] *Department of Materials Science and Metallurgy, University of Cambridge, 27 Charles Babbage Road, Cambridge, CB3 0FS, United Kingdom*

Abstract

Efficient separation of increasingly complex oil–water mixtures demands advanced materials capable of adaptive, on-demand performance under diverse environmental conditions. Conventional single-function separation materials often fail to meet these challenges, particularly in achieving controllable separation in dynamic or contaminated environments. This highlights the pressing need for intelligent materials to help mitigate global water pollution and oil scarcity. In this study, a series of reversible dual-stimuli-responsive polymers were synthesised via a straightforward one-step reversible addition-fragmentation chain transfer (RAFT) polymerisation method. Incorporating azobenzene-based photoswitches and pH-responsive units, these polymers exhibit significant and reversible responsiveness to both UV irradiation and pH variation. When coated onto stainless steel wire

meshes, the resulting reusable membranes demonstrated excellent performance in separating oil–water mixtures. Under alkaline conditions or upon irradiation with 445 nm light, the membranes exhibited a maximum water contact angle of approximately 140°. In contrast, under acidic conditions or 365 nm UV exposure, the membranes switched to a superhydrophilic state with a contact angle of around 6°, resulting in a maximum contact angle variation of 134°. Additionally, antibacterial assays revealed a maximum inhibition rate of 75.1%, confirming the coatings' potential effectiveness in biological environments. This work demonstrates a bright strategy for designing multifunctional and controllable oil–water separation coatings, with potential applications in complex, real-world settings requiring both separation efficiency and antibacterial properties.

keywords: Azobenzene-based photoswitches, pH-responsive units, RAFT, Hydrophilic lipophilic reversible conversion, Oil–water separation.

1. Introduction

Nowadays, due to rapid global population growth and increasing industrialization, large volumes of oily wastewater generated from industrial discharges and oil spills pose significant threats to the ecological environment[1]. Effective oil-water separation technology is crucial for addressing these pollution challenges. Compared to traditional oil-water separation techniques, such as gravity sedimentation and high-speed centrifugation, membrane separation technology has emerged prominently over the past two decades due to its simplicity and low energy consumption[2-5]. By simply passing oily wastewater through special designed membranes, oil can be effectively separated from water.

Oil–water separation membranes with single wettability functionality have been

developed through a variety of approaches, ranging from the use of metals with functional polymer surfaces to advanced polymer material[6]. One notable example involves the reaction of stainless steel with dynamically eroded TiO_2 microspheres under acidic conditions, forming a petal-like superhydrophobic Fe/TiO_2 film that enables efficient oil–water separation alongside photocatalytic dye degradation[7]. In addition to metal-based systems, microporous polymers have emerged as versatile alternatives. A conjugated microporous polymer membrane was synthesized via Sonogashira–Hagihara cross-coupling of 1,3,5-triethynylbenzene and 2,6-dibromophenol, then electrospun with polyvinylidene fluoride and polymethyl methacrylate solutions to create a functional composite for efficient oilwater separation[8]. Another design featured a modified hydrolyzed polyacrylonitrile film, imparting photocatalytic self-cleaning and antibacterial capabilities[9]. Covalent organic frameworks (COFs) represent another promising class of membrane materials. Using a filter assembly method, COF-based carbon nanofiber films with switchable wettability have been fabricated, allowing for selective oil–water transport[10]. Furthermore, as interest in nanofiber membranes continues to grow, electrospun nanofiber membranes incorporating hydrated manganese dioxide nanoparticles have been developed for ultrafiltration and the treatment of synthetic oil solutions[11, 12].

However, as oil–water mixtures become increasingly complex—encompassing light/heavy oil combinations, oil-in-water emulsions, and water-in-oil emulsions—conventional single-function membranes, such as those described above, often struggle to deliver efficient, adaptable, and sustainable separation. This has spurred interest in intelligent coating materials that can be easily deposited onto substrates, offering scalable fabrication and cost-effective deployment for industrial applications. To address these challenges, reversible

dual-stimuli-responsive polymer coatings present an appealing solution[13-15]. Light-responsive systems, in particular, are attractive due to their rapid switching, simplicity, non-contact operation, and ease of integration with portable light sources[16-20]. In parallel, pH-responsive functionalities enable adaptability in chemically diverse environments, particularly where substances must remain stable under acidic or alkaline conditions[21-23]. The combination of light and pH responsiveness thus offers a promising approach to developing next-generation intelligent oil–water separation materials, with broad applicability in complex and dynamic environments, helping to combat global water pollution and oil scarcity.

In this study, a series of reversible dual stimuli-responsive polymers were synthesized as coating materials, incorporating azobenzene-based photoswitches and pH-responsive units. These polymers were prepared using a straightforward, one-step reversible addition–fragmentation chain transfer (RAFT) polymerization method. Density functional theory (DFT) calculations were employed to investigate the polymerization reaction mechanism. Oil-water separation tests demonstrated that these azobenzene polymers, when uniformly coated onto stainless steel wire meshes, exhibited excellent separation capabilities for various oil-water mixtures, achieving a separation efficiency of up to 97.6% for water-petroleum ether mixtures. The coated membranes exhibited responsive wettability, reaching a maximum water contact angle of approximately 140° under alkaline conditions and 445 nm irradiation, while rapidly transitioning to superhydrophilic (water contact angle ~6°) under acidic conditions and 365 nm UV irradiation. Simultaneously, the maximum oil repellency angle reached approximately 145°, highlighting the membranes' excellent dual responsiveness and repeatability under UV and pH stimuli for controllable separation purpose. Additionally, given that oily wastewater is often present in bacterially contaminated environments, the antibacterial performance of a polymer membrane with excellent stimuli-responsive

properties was evaluated against four representative microbial species: Candida albicans, Staphylococcus aureus, Bacillus subtilis, and Pseudomonas aeruginosa. The membrane exhibited notable inhibitory effects, with rates of up to 74.2%, 75.1%, 52.1%, and 67.2% against these strains, respectively. Thus, this work highlights the developed oil-water separation coating materials as promising candidates for sustainable and efficient performance, offering multi-responsive control and adaptability in complex, biologically contaminated environments.

2. Experimental

2.1. Reagents and chemicals

Dimethyl sulfoxide (DMSO) and tetrahydrofuran (THF) were purchased from Xilong Science Co., LTD. China. Methyl acrylyl chloride (MC), p-cyananiline phenol, sodium hydroxide, sodium bicarbonate, sodium nitrite, triethylamine, ammonium persulfate (APS), azobisisobutyronitrile (AIBN), 3-chloropropanol, 6-chlorohexanol, 8-chlorooctanol, potassium iodide (KI), 2-hydroxyethyl methacrylate (HEMA), dimethylaminoethyl methacrylate (DMAEMA) were purchased from Macklin Reagent Net, China. Cumyl dithiobenzoate (CDB), 11-dodecenoic acid from Aladdin Biotechnology Co., LTD, China. 304 stainless steel mesh (300 meshs, the aperture is about 50 microns) was purchased from Hebei Weijia Metal Mesh Co., LTD. China. Trypticase Soy Broth (TSB), Candida albicans, Staphylococcus aureus, Bacillus subtilis and pseudomonas aeruginosa were purchased from Ningbo Mingzhou Biotechnology Co., LTD. China. All reagents are used directly without further purification.

2.2. Characterization methods

The morphology of the samples was analyzed using a field emission scanning electron microscope (SEM; GeminiSEM 500, Zeiss, Germany). The structural composition of all products was characterized using Fourier transform infrared (FTIR) spectroscopy within a wavenumber range of 4000–400 cm^{-1} and a resolution of 2 cm^{-1}. A 365 nm ultraviolet lamp (20W) was used to provide UV illumination, while a 445 nm LED lamp (20W) served as a visible light source for wavelength-specific experiments, with natural light used as a control for comparison.

Azobenzene monomers with varying carbon chain lengths were dissolved in ethanol (1.5 g L^{-1}), and their *cis-trans* isomerization behavior was analyzed using a UV-VIS spectrophotometer (METASH UV-5200PC). The isomerization was induced by exposure to a 365 nm ultraviolet lamp (20 W) for *trans*-to-*cis* conversion, followed by a 445 nm LED lamp (20 W) and natural solar light. The latter was tested under diffuse sunlight conditions in Lanzhou, a city in central Gansu Province, China, known for its abundant solar energy resources, with an annual total solar radiation of approximately 5400–6100 MJ $year^{-1}$[24].

2.3. Synthesis of polymers and oil-water separation membrane preparation

The synthesis routes for the azobenzene intermediates, monomers, and polymers with varying chain lengths, based on the modified synthetic protocols, are illustrated in Scheme 1. These routes include **Intermediate 1** to **Intermediate 6**, **Monomer 1** to **Monomer 5**, and **Polymer 1** to **Polymer 4**. The synthesis route (a) and (b) can mainly be divided into three steps: (1) diazo-coupled reaction, (2) esterification reaction, and (3) polymerization reaction. Route (a) stands for the synthesis way of **Polymer 1**, and (b) stands for **Polymer 2-4**. Route (c) stands for the synthesis way of **Monomer 5** and **Polymer 5**. Route (d) represents another way to synthesize **Monomer 4**.

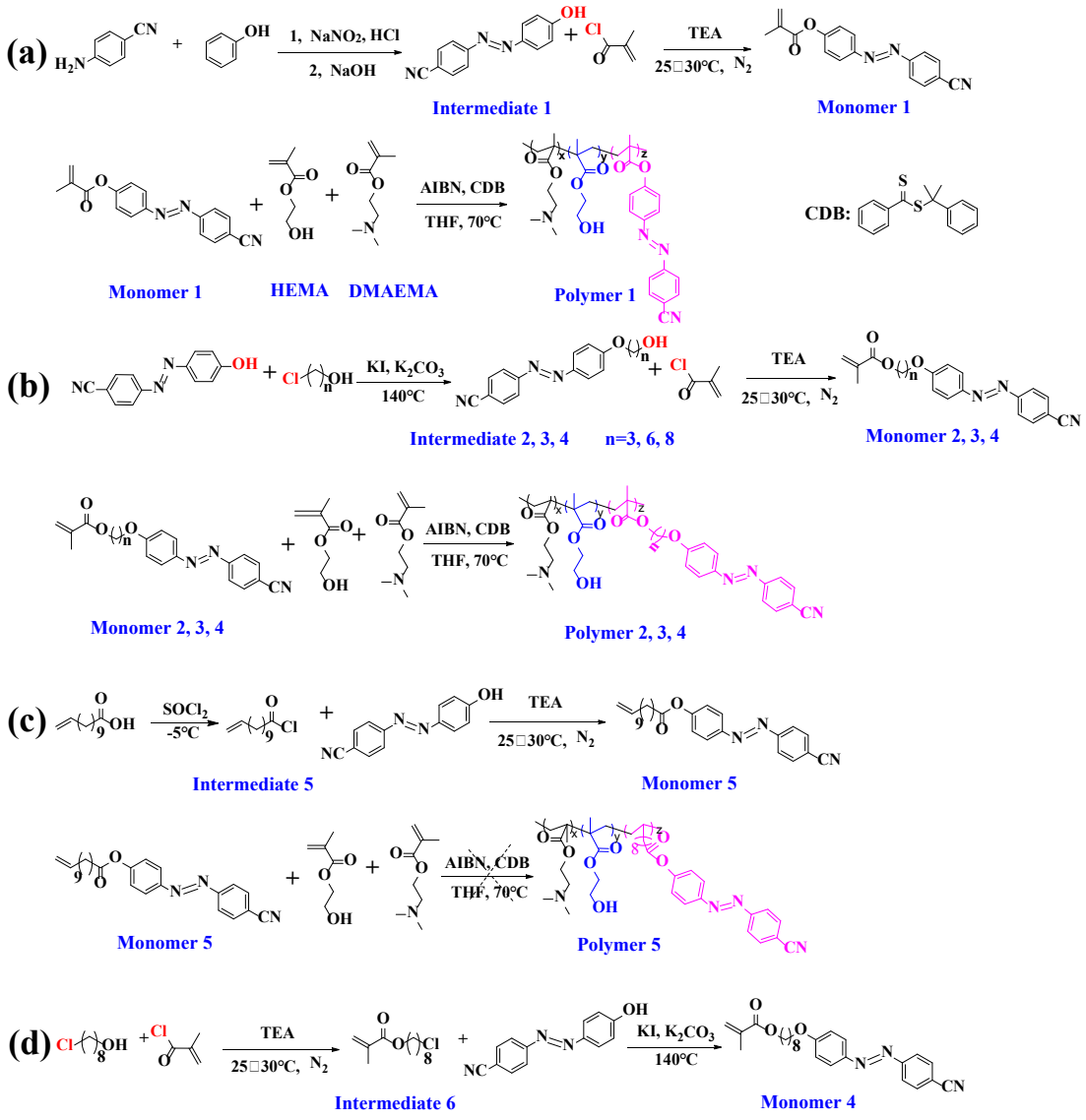

Scheme 1 Synthesis route of photo-responsive functional monomers and polymers.

After the above multi-step reactions, viscous polymers that are insoluble in solvents were obtained. The adhesive polymers were uniformly coated on the stainless steel meshes and dried in a vacuum drying oven at 60℃ for 4h to obtain oil-water separation membrane, the polymers hardened and firmly covered the stainless steel mesh wire. The membrane was pre-wetted with water prior to each oil–water separation test.

2.4. Computational methods

DFT calculations were performed to investigate the structural and electronic properties of the system. All computations were conducted using the Gaussian16 program, applying tight convergence criteria for both the self-consistent field (10^{-10} a.u.) and geometry optimization (10^{-5} a.u.)[25]. The B3LYP hybrid exchange-correlation functional, combined with the 6-31G(d,p) basis set, was employed to analyze the reaction mechanisms[26]. The calculations involved optimizing the geometries of various reactants, metastable intermediates, and products. Energy changes and vibrational frequencies for each reaction step were computed to confirm zero imaginary frequencies, ensuring the identification of stable structures. Additionally, the binding energy of the initiation RAFT process and the radical transfer process were determined. The initial structure of the reaction intermediate was estimated by scanning the relaxation potential energy surface along appropriate internal coordinates, allowing for the evaluation of the overall energy changes throughout the reaction pathway[27].

3. Results and discussion

3.1. Structural characterization of all precursors and final reversible dual stimuli-responsive polymers

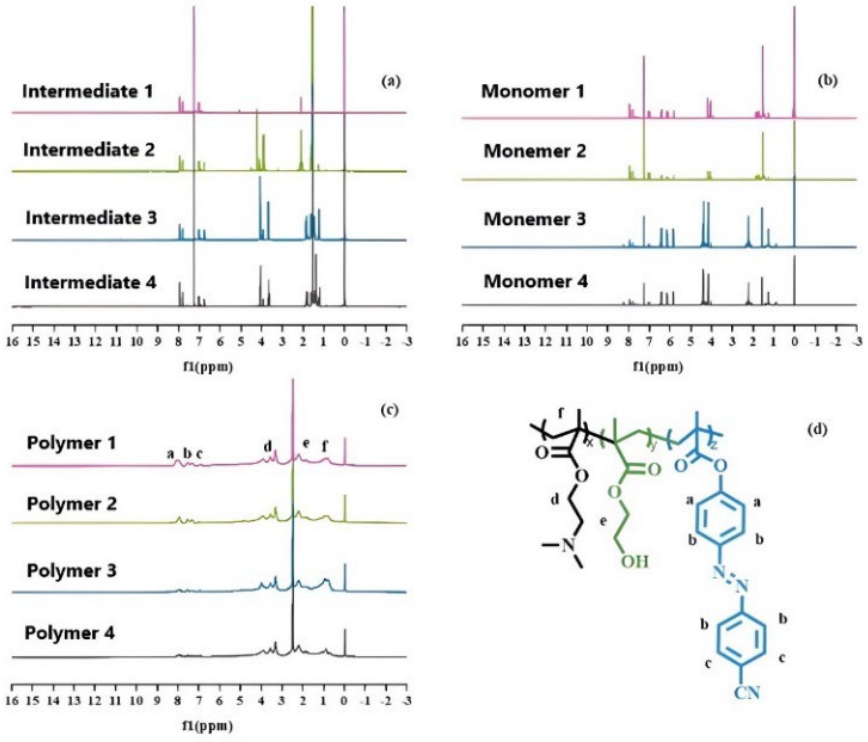

Figure. 1 ^{1}H NMR spectra of the synthesized materials with varying chain lengths: (a) intermediate, (b) monomers, (c) polymers, and (d) structural formulas of **Polymer 1**.

The proton nuclear magnetic resonance (^{1}H NMR) analysis for each step of the synthesis process, along with the ^{1}H NMR spectrum of the final synthesized polymers, is presented in Figure 1. Figure 1a illustrates hydroxy-azobenzene intermediates with varying carbon chain lengths. In the ^{1}H NMR spectrum, the characteristic peaks corresponding to aromatic protons of the azobenzene core appear at 6.96 ppm, 7.00 ppm, 7.33 ppm, and 7.91 ppm, while the methylene-linked hydrogen adjacent to oxygen exhibits distinct peaks at 3.68 ppm and 4.06 ppm. Notably, these peaks are absent in the monomers, distinguishing the intermediate stage from subsequent structures. Finally, the signals corresponding to saturated alkyl groups appear within the 1.2–2 ppm chemical shift range. Figure 1b presents the monomers with different carbon chain lengths. Compared to the intermediates in Figure 1a, there is a

noticeable increase in characteristic peaks associated with double-bonded hydrogen atoms, specifically at 6.13 ppm and 6.40 ppm. The integrated areas of these characteristic peaks align well with the expected molecular structures, confirming the successful synthesis of azophenyl monomers with varying carbon chain lengths. Figure 1c displays the ^{1}H NMR spectrum of the synthesized final polymers, with **Polymer 1** used as a representative example. The characteristic peaks at 7.99 ppm, 7.81 ppm, 7.35 ppm, and 6.98 ppm correspond to protons a, b, c, and d, respectively, on the azobenzene backbone, as annotated in the structural formula in Figure 1d. The hydrogen adjacent to the oxygen atom (labeled e) is identified at 4.82 ppm, while the hydrogen adjacent to the nitrogen atom (labeled f) also appears at 4.82 ppm. The remaining peaks within the 1.0–2.4 ppm range correspond to saturated methylene and methyl groups, further validating the polymer structure. Overall, these NMR results confirm the successful stepwise synthesis of the target azophenyl polymers with different carbon chain lengths.

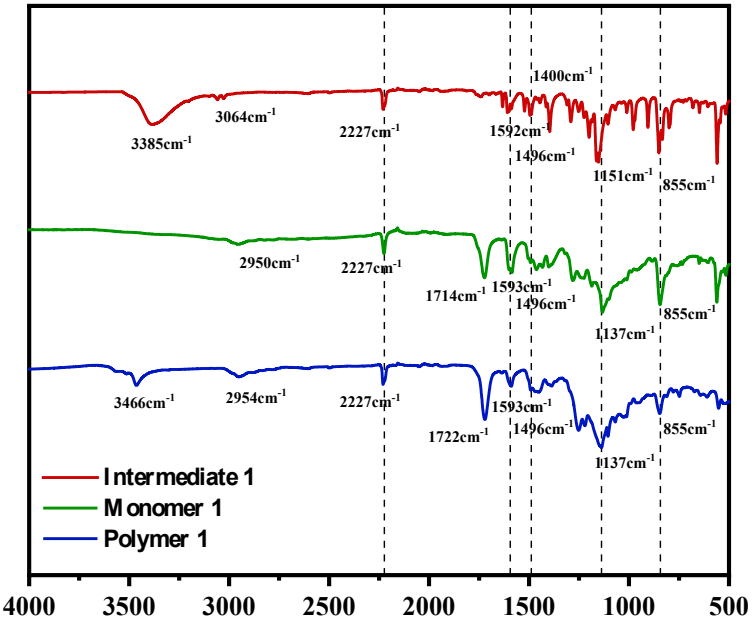

Figure. 2 FTIR spectra of **Intermediate 1**, **Monomer 1**, and **Polymer 1**. Dashed lines indicate the common characteristic peaks.

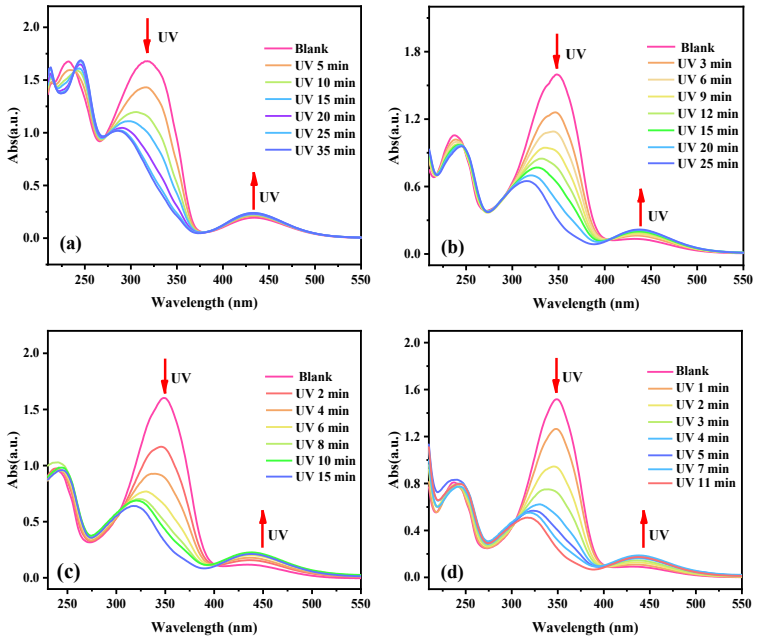

Figure. 3 UV-Vis spectra of **Monomer 1–4** (a–d) at different time intervals under ultraviolet irradiation.

In addition to NMR characterization, the structural transformation during the polymerization process was confirmed through FTIR spectral analysis of Intermediate 1, **Monomer 1**, and **Polymer 1**, as shown in Figure 2. In the spectrum of Intermediate 1, the stretching vibration peak of the hydroxyl (-OH) group appeared at 3385 cm^{-1}, with its in-plane bending vibration observed at 1400 cm^{-1}. As the polymerization proceeded, the disappearance of the -OH peak and the emergence of carbonyl (-C=O) and ether (-C-O-C) bonds indicated successful monomer conversion. The stretching vibration peaks of the C=O group were recorded at 1714 cm^{-1} and 1722 cm^{-1} for **Monomer 1** and **Polymer 1**,

respectively, while the ether bond vibration was observed at 1137 cm^{-1}. Additionally, characteristic peaks, such as C≡N stretching vibration at 2227 cm^{-1}, benzene ring skeletal vibrations at 1592 cm^{-1}, and substituted aromatic out-of-plane bending vibrations at 855 cm^{-1}, were consistent throughout the reaction, aligning with the expected FTIR spectrum of the target polymer. These results provided strong evidence supporting the successful polymerization and formation of the designed polymer structures.

3.2. Spectral characterization of Monomer 1-4

Figure 3 presents the UV absorption spectra of ethanol solutions containing different monomers under ultraviolet (UV) irradiation. The characteristic absorption peak of azobenzene compounds is primarily attributed to the π-π* transition within the 280–380 nm range[28]. With increasing UV exposure time, the intensity of this π-π* absorption peak gradually decreases, accompanied by a progressive blue shift in the absorption wavelength of the monomers. Simultaneously, the n-π* transition peak at approximately 440 nm exhibits a steady increase in absorbance. These spectral changes can be clearly attributed to the UV-induced *trans*-to-*cis* isomerization of the azobenzene units. Figure 4 illustrates the UV absorption spectra of **Monomer 1** under 445 nm visible light irradiation. A comparison of the spectra reveals that the *cis*-*trans* isomerization of azobenzene is a fully reversible process, enabling rapid reconversion at specific wavelengths. Notably, 95% of the isomerization can be completed within 15 seconds at 445 nm, demonstrating a highly efficient back-conversion. This observation confirms the reversible transformation of *cis*-*trans* isomers, which influences the molecular polarity and further validates the reversible wettability of the polymer coatings.

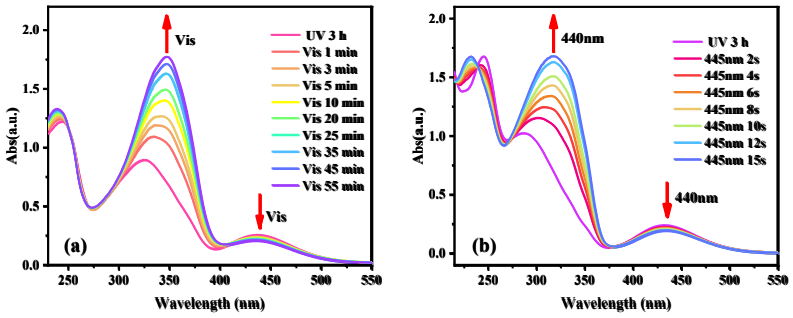

Figure. 4 UV absorption spectra of **Monomer 1** at different time intervals under (a) natural light and (b) 445 nm visible light irradiation.

3.3. DFT investigation of the unsuccessful polymerization mechanism of Monomer 5

As showing in Scheme 2, RAFT mechanism consists of several key stages: initiator activation and propagation (step a), RAFT pre-equilibrium (step b), re-initiation and further propagation (step c), RAFT main equilibrium (step d), and termination of the polymerization. Following initiator activation, the resulting radical species add to the RAFT agent (chain transfer agent, such as CDB), initiating an equilibrium between active and dormant species (steps b and d). The chain transfer steps that underpin the RAFT mechanism are degenerate, involving a reversible exchange of the functional chain-end group—typically a thiocarbonylthio moiety (Z−C(=S)S−R)—between dormant chains and propagating radicals.

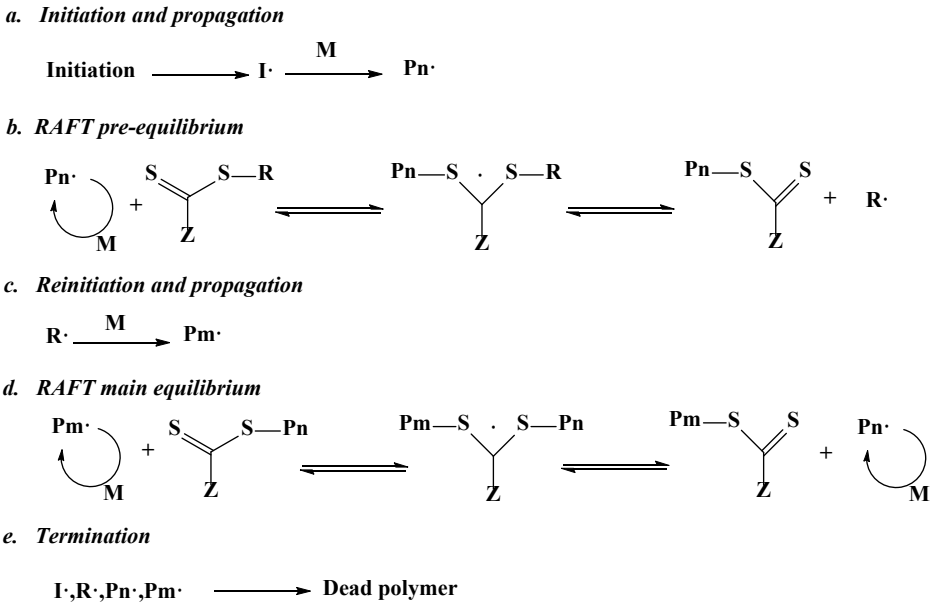

Scheme 2 Mechanism of RAFT polymerization.

Subsequently, **Monomers 1–4** were successfully polymerized via RAFT polymerization to yield **Polymers 1–4**, respectively. In parallel, **Monomer 5** was synthesized with the intention of producing **Polymer 5** under identical conditions, as illustrated in Scheme 1. However, no polymerization reaction occurred. This is primarily due to the low reactivity of vinyl groups, which are inherently weak in radical polymerization. Additionally, in the polymerization process of ethylene-based monomers, the growing free radical lacks conjugation and stabilizing functional groups, making it highly unstable. This instability leads to poor reactivity of dormant intermediates, ultimately inhibiting successful RAFT polymerization[29]. For RAFT polymerization to be effective, the rate of addition-fragmentation equilibrium must be higher than the propagation rate, ensuring controlled monomer addition per activation cycle. Ideally, this results in uniform polymer chain lengths across all chains at a given time[30, 31]. However, due to the poor stability of **Monomer 5**'s propagating radical, this equilibrium is disrupted, leading to premature termination of

polymerization.

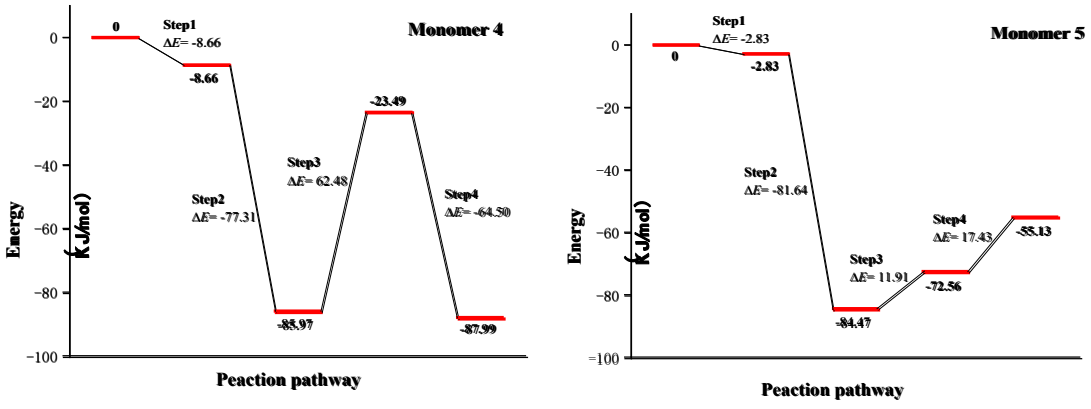

Figure. 5 DFT-calculated energy diagram of the polymerization reaction of **Monomer 4** and **Monomer 5.**

To further investigate why **Monomer 5** cannot undergo polymerization, we compared it with **Monomer 4**, which shares the same carbon chain length and molecular formula but differs in structure. The energy changes of both monomers during the polymerization process were calculated via DFT, as shown in Figure 5. The calculations indicate that in the first two reaction steps (Step 1 and Step 2), the energy changes for both monomers are similar, with a decreasing system energy. However, in the last two steps, the energy profile diverges: for **Monomer 4**, the energy initially increases before ultimately decreasing, leading to a final product with the lowest energy. In contrast, the energy of **Monomer 5** continues to increase throughout the last two reaction steps, preventing further progression of the polymerization process. The overall energy change (ΔE) for **Monomer 4** from Step 1 to Step 4 during the RAFT polymerization was calculated as -87.99 kJ/mol, whereas for **Monomer 5**, it was only -55.13 kJ/mol. Since the RAFT polymerization of **Monomer 4** results in a stable product, this energy difference suggests that the unfavorable energy landscape of **Monomer 5** prevents it

from undergoing successful polymerization. These findings emphasize the need for structural modifications in low-activity monomers like **Monomer 5**. Future approaches may focus on introducing stabilizing functional groups or modifying the RAFT agent to improve polymerization efficiency and enable successful polymer formation.

3.4. Dual-stimuli responsiveness characterization of the coated stainless steel mesh membrane

To evaluate the oil–water separation performance of the reversible dual stimuli-responsive polymers and investigate the effect of azobenzene monomer alkyl chain length on wettability, the four synthesised polymers were uniformly coated onto stainless steel meshes with a pore size of 50 μm. The polymer chains interwove and wrapped around the stainless steel wires, enabling strong adhesion and uniform coverage across the mesh surface. The coated meshes were then placed in an oven at 60°C for 24 hours to ensure complete film formation before conducting the water contact angle tests. For the contact angle measurements, 5 μL water droplets were deposited onto the coated surfaces, and the average values were obtained from five independent measurements conducted under the same conditions. The measurement error for the contact angle tests was ±2.3°. The water contact angles of **Polymers 1–4** at different condition are presented in Figure 6a. As observed, the hydrophobicity of the polymer coatings exhibited a slight increase with an increase in carbon chain length, leading to a small rise in the contact angle at the hydrophobic state by approximately 2°–6°. However, this change was not particularly significant, likely due to the already substantial total carbon length of the polymer, which dominates the surface wettability behavior. As Polymer 1 exhibits the largest hydrophobicity, further investigation with varies pH was conducted. Figure 6b and 6c presents the contact angle variation of the water-oil

separation mesh prepared with **Polymer 1** under different lighting conditions and buffer solutions of pH = 3, 7 and 10. The "Blank" in Figure 6c represents the contact angle of the polymer coating without any treatment. The test of pH response performance refers to soaking the polymer coating in buffer solutions with different pH values for 1 hour, drying it, and then irradiating it under different lighting conditions to measure its contact angle. The pH responsiveness is attributed to the tertiary amine groups within the polymer, which undergo protonation in acidic conditions, increasing hydrophilicity, and deprotonation in alkaline conditions, leading to hydrophobicity. This results in a decreased contact angle in acidic environments due to enhanced hydrophilicity, while an increase in pH leads to a rise in contact angle due to deprotonation-induced hydrophobicity, confirming the polymer's pH-responsive wettability behavior.

To assess the reversible switching ability of the polymer coating, three cycles of pH, UV, and combined pH & UV stimulation were performed, with results shown in Figure 6d. The findings demonstrate that UV exposure induces a stronger response compared to pH changes, while the combined pH & UV dual-stimulus exhibits the most pronounced effect. Specifically, pH stimulus alone induces a contact angle change of 41°, UV stimulus results in an 100° change. Under alkaline conditions or 445 nm light irradiation, the membranes achieved a maximum water contact angle of ~140°, which switched to superhydrophilic behaviour (~6°) under acidic conditions or 365 nm UV exposure. The combination of these stimuli resulted in a maximum contact angle variation of 134°.

In complex oil-water mixture environment, the membrane sometimes need be immersed in the mixture for a long period of time, therefore, further evaluation of the water-oil separation membrane performance of the polymer coating was conducted by immersing the polymer-coated steel mesh in water for 10 minutes to mimic the immersing condition,

followed by testing the oil-phobic contact angle variation using petroleum ether. We have evaluated the cyclic stability of the polymer membrane over a sufficient number of cycles (10 cycles), and the corresponding results are presented in Figure 6e, the maximum oil contact angle reached 145°, while the minimum decreased to 60°. Similarly, the maximum and minimum water contact angles were recorded as 138° and 6° under dual stimulation, respectively, resulting in a total water contact angle variation of 132°. These results confirm the polymer coating's excellent water-oil separation capability and its ability to switch between hydrophobic and hydrophilic states effectively.

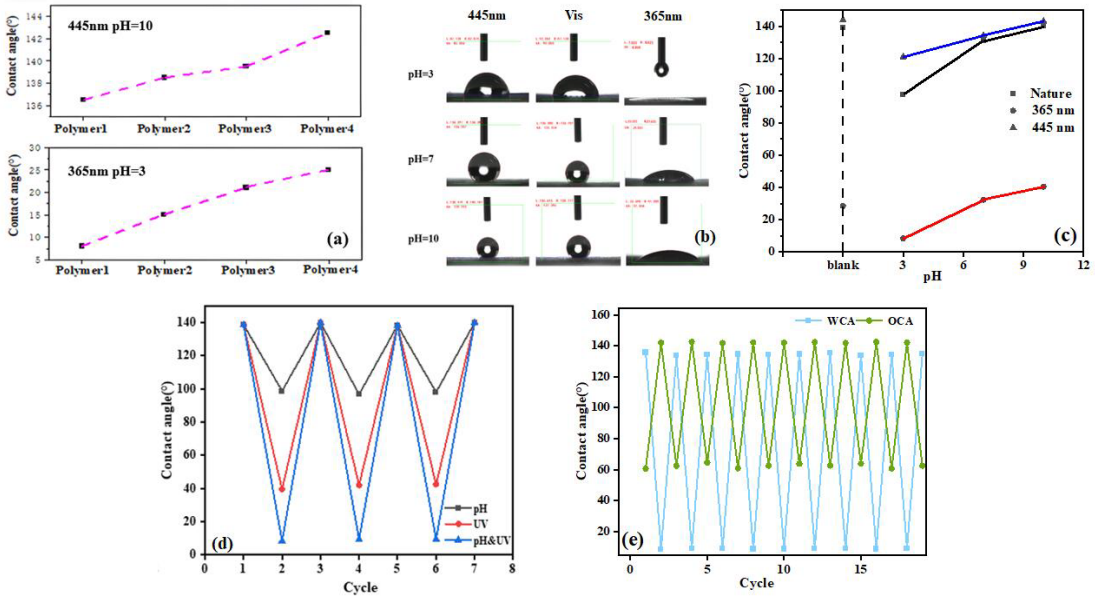

Figure. 6 Wettability response of polymer coatings under pH and light stimuli. (a) Contact angles of polymer coatings with different carbon chain lengths at pH = 7. (b) Water contact angles of **Polymer 1** coatings under different pH and illumination conditions. (c) Contact angle variation with pH under the same light source. (d) Reversible cyclic changes in contact angle under repeated dual stimuli. (e) Reversible cyclic changes in water and oil contact angles under repeated dual stimuli, demonstrating the coating's stability and responsiveness.

In addition to measuring the water contact angles under air conditions, we also performed underwater oil contact angle measurements on the polymer-coated oil–water separation membranes prepared with polymers 1–4. 5 μL oil droplets were deposited onto the coated surfaces under water, and the average values were obtained from five independent measurements conducted under the same conditions. As shown in Figure 7, the underwater oil contact angles exhibit slight differences across the four polymer systems. Upon exposure to 445 nm light, the membranes gradually transition from an oleophobic to an oleophilic state (i.e., from hydrophilic to hydrophobic). Conversely, irradiation with 365 nm UV light reverses this transition, shifting the membrane from oleophilic back to oleophobic (i.e., from hydrophobic to hydrophilic). These results confirm that the membrane's wettability toward oil and water can be intelligently and reversibly regulated by external stimuli, enabling dynamic and on-demand oil–water separation.

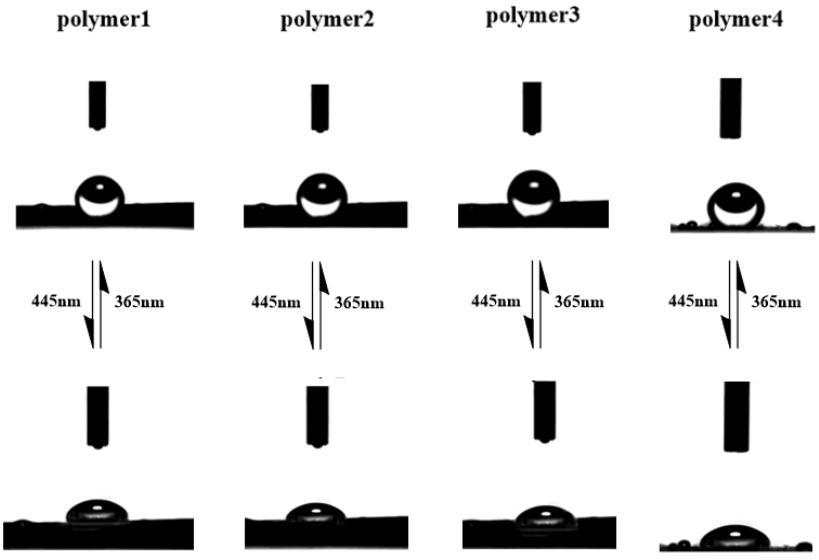

Figure. 7 Contact angle of oil droplets with polymer 1-4 coatings under water.

3.5. Real Water-Oil Separation Performance test of the Polymer-Coated Stainless steel Mesh

To evaluate the water-oil separation capability of the polymer-coated stainless steel mesh, circular samples with a diameter of 3.1 cm were prepared for testing. A dyed water sample was created by dissolving 1 mg of methyl orange in 200 mL of distilled water, which was then mixed in equal volume with petroleum ether to form a water-oil mixture. The prepared mixture was poured into a funnel containing the polymer-coated stainless steel mesh, and the oil-water separation system was simulated by suction filtration at room temperature and pressure of 0.005 Mpa. By calculating, the water flux and oil flux of the polymer membrane were about 1.77×10^4 $L\cdot m^{-2}\cdot h^{-1}$ and 7.88×10^3 $L\cdot m^{-2}\cdot h^{-1}$, respectively. Figure 8a shows the separation process under natural conditions. The images, taken at three time points (before separation, 30 seconds after separation, and 1 minute after separation), demonstrate that the clarified petroleum ether successfully passed through the mesh into the bottom container while the orange aqueous solution remained at the top, achieving efficient separation. Figure 8b presents the separation process after the polymer-coated stainless steel mesh was irradiated with 365 nm UV light for 6 hours. Unlike the natural state separation, the UV-treated mesh caused an opposite separation behavior—where the clarified petroleum ether remained above the funnel while the orange aqueous solution passed through, demonstrating a reversible switch in wettability. To further assess the separation performance of the polymer-coated stainless steel mesh across different oil-water mixtures, additional tests were conducted using hexane, dimethylsilicone oil, vegetable oil, and petroleum ether mixed with water. As illustrated in Figure 8c, the separation efficiency for petroleum ether in the natural state reached 97.1%. After UV irradiation, the separation efficiency of water in the water-dimethylsilicone oil mixture increased to 97.6%, with overall separation efficiencies exceeding 87% across all tested oil-water mixtures. These results confirm that the polymer-coated mesh exhibits excellent water-oil separation performance with high efficiency, making

it suitable for practical applications in diverse environments.

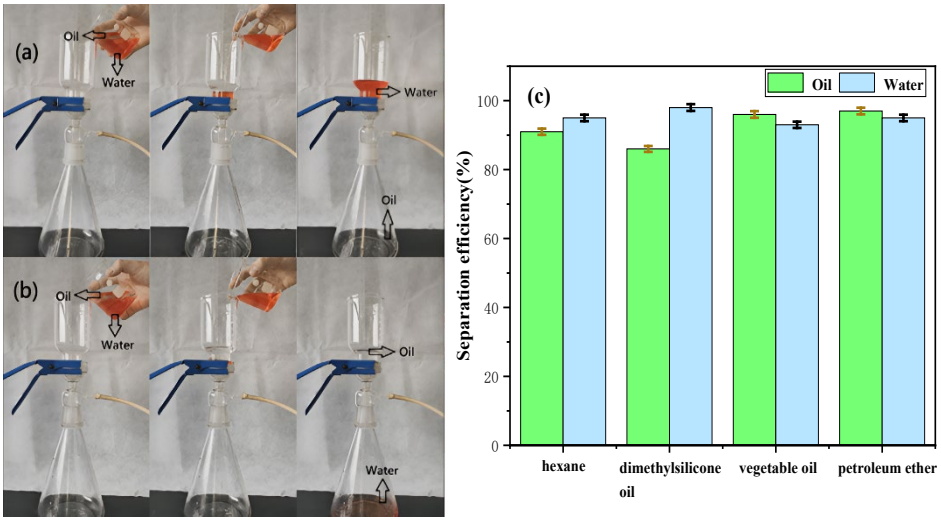

Figure. 8 Water-oil separation process and efficiency. (a) Schematic representation of the water-oil separation process in its natural state. (b) Water-oil separation process after 4 hours of UV light irradiation, demonstrating the reversible wettability switch. (c) Separation efficiency of different water-oil mixtures, highlighting the material's adaptability and high separation performance.

3.6. Polymer adhesive test on stainless steel mesh

To finally evaluate the durability and stability of the polymer coating on the stainless steel mesh and assess its mechanical robustness under repeated deformation, the coated mesh was subjected to 10 folding cycles. The surface morphology was compared with a blank mesh to determine the impact of mechanical stress on coating integrity.

As shown in Figure 9a, the uncoated stainless steel mesh exhibited a smooth and porous surface structure. However, after applying the polymer coating, a dense and uniform polymer film was formed on the surface, as illustrated in Figure 9b, enabling controlled water-oil separation.

To assess mechanical durability, the coated mesh was repeatedly folded 10 times by hand. As seen in Figures 9c and 9d, slight kink marks and convex deformations were observed on the mesh structure due to mechanical stress. However, the polymer film remained intact within the pores, demonstrating strong adhesion to the substrate.

Following the mechanical stress test, the coated stainless steel mesh underwent a cyclic water-oil separation test to evaluate performance retention. The results confirmed that the separation efficiency remained unchanged, indicating excellent mechanical stability and adhesion of the polymer coating. This suggests that the water-oil separation mesh is highly durable, making it well-suited for practical applications in complex environments where mechanical stress and repeated usage are expected.

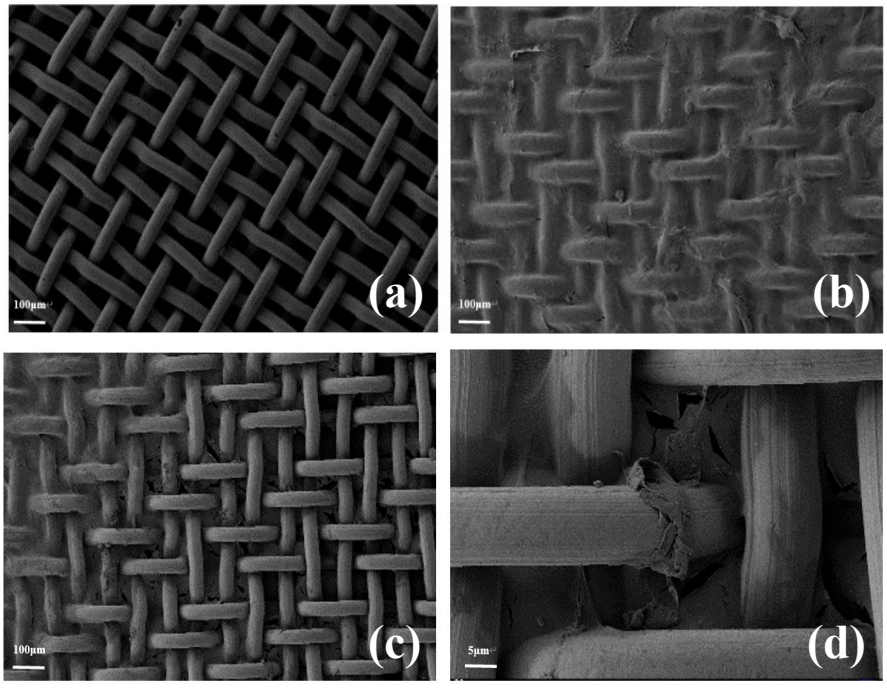

Figure.9 SEM images of the water-oil separation mesh. (a) Blank stainless steel mesh before coating. (b) Stainless steel mesh coated with the polymer, showing uniform coverage. (c) Polymer-coated stainless steel mesh after being folded 10 times. (d) Zoomed image of picture (c).

3.7. Antibacterial Performance of the Oil-Water Separation Polymer

Oily wastewater typically exists in contaminated environments containing abundant bacteria. To evaluate the antibacterial properties of the oil-water separation polymer material under complex application conditions, four representative bacterial species—Candida albicans, Staphylococcus aureus, Bacillus subtilis, and Pseudomonas aeruginosa—were selected. For each bacterial species, blank Petri dishes containing only DMSO and experimental dishes containing polymer-DMSO solutions at a concentration of 20 g L^{-1} were prepared. Each bacterial strain was cultured separately in 10 mL of TSB, and the resulting bacterial suspensions were individually transferred into the prepared Petri dishes. All dishes were subsequently incubated at 27 °C for 20 hours.

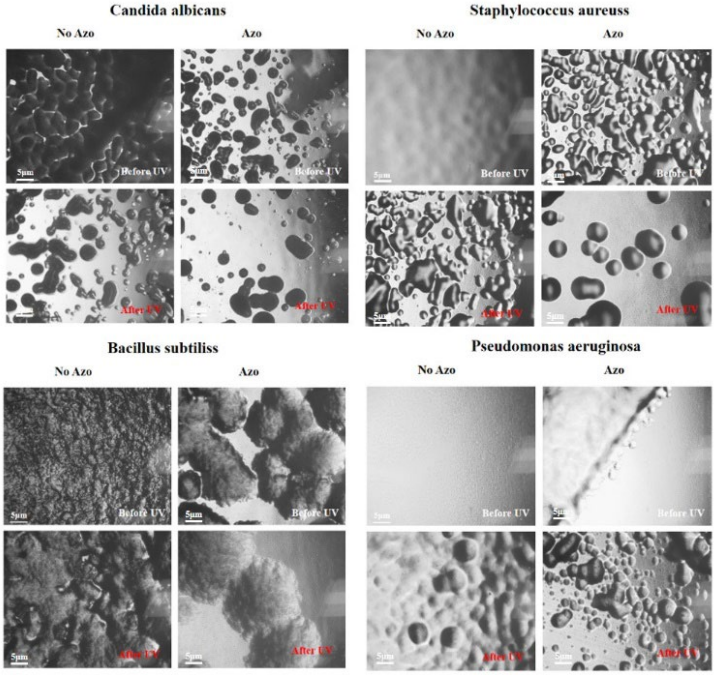

Figure. 10 Growth comparison of four different bacterial colonies on blank and polymer-containing Petri dishes. The diagram illustrates the bacterial proliferation in the absence of the polymer and the inhibitory effect of the polymer coating on colony formation.

After incubation, bacterial growth was quantified by measuring absorbance at 600 nm (A600), assuming a standard optical density (OD) equivalence of 1 OD = 1×10^{8} CFU mL^{-1} (Figure 10). As shown in Figure 10, bacterial colony activity in Petri dishes containing polymer solutions was lower compared to those containing only DMSO, with the most pronounced effect observed for Staphylococcus aureus. After subsequent exposure to UV irradiation at 365 nm for 10 minutes, colonies in dishes without polymer exhibited only a slight decrease, while colonies in polymer-containing dishes showed a substantial decline. These observations confirm the unique photofluidization properties of azobenzene molecules within the polymer.

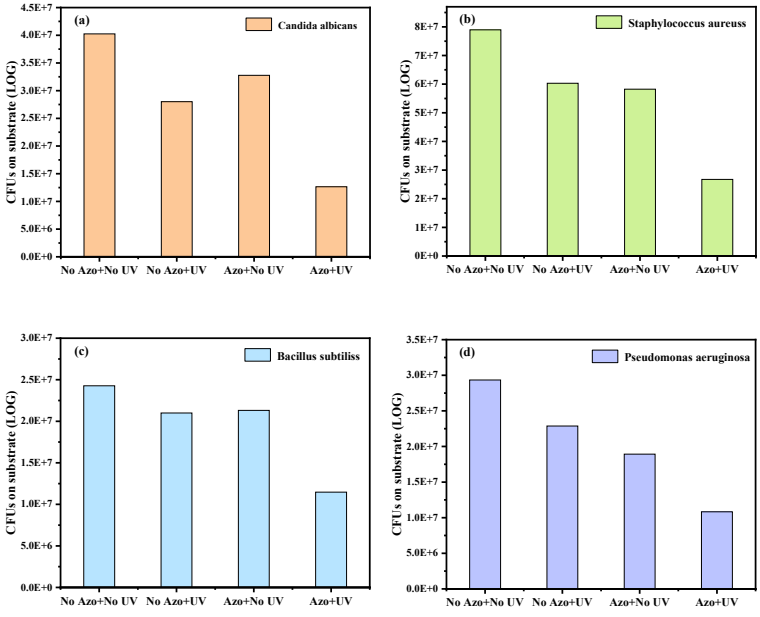

Figure. 11 Bioactivity analysis of four bacterial colonies under different growth conditions. (a) Candida albicans, (b) Staphylococcus aureus, (c) Bacillus subtilis, and (d) Pseudomonas aeruginosa. The figure demonstrates bacterial viability in the presence and absence of the polymer coating, highlighting its antibacterial effectiveness.

Photofluidization refers to the rapid, reversible *trans-cis-trans* isomerization of azobenzene groups under light exposure. When exposed simultaneously to multiple wavelengths of light, azobenzene molecules undergo transient surface softening and flow, accompanied by a temporary reduction in Young's modulus. This photomechanical effect enables the polymer surface to disrupt biofilms mechanically, provided the induced force exceeds the cohesive strength within the biofilm and its adhesion strength to the substrate. Consequently, the polymer demonstrates enhanced antibacterial performance under UV irradiation. The quantified bacterial populations under these experimental conditions are presented in Figure 11. The polymer membranes showed inhibitory rates against Candida albicans, Staphylococcus aureus, Bacillus subtilis, and Pseudomonas aeruginosa of 74.2%, 75.1%, 52.1%, and 67.2%, respectively. Thus, the oil-water separation coating offers promising potential for prolonged effectiveness in diverse biological environments.

4. Conclusions

In this study, a series of p-cyanoazobenzene monomers with varying alkyl chain lengths were successfully synthesized, and corresponding reversible dual stimuli-responsive polymers were developed via RAFT block polymerization for use as oil–water separation coating materials. The coating, applied onto stainless steel wire meshes, exhibited excellent reversible wettability under both UV and pH stimuli, with water contact angles reaching 140° and 6°, respectively. In addition to measuring the water contact angles under ambient air conditions, underwater oil contact angle measurements were conducted on the polymer-coated oil–water separation membranes. The results demonstrate that the membranes' wettability toward oil and water can be intelligently and reversibly modulated by external stimuli, enabling dynamic

and on-demand oil–water separation. Regarding its cyclability, the function remained stable even after multiple cycles, demonstrating long-term durability. Beyond its outstanding oil-water separation efficiency of up to 97.1%, the coating also exhibited remarkable mechanical stability and antibacterial performance, with a maximum bacterial inhibition rate of 75.1%. The antibacterial properties were confirmed through tests against four representative bacterial species, highlighting its potential for maintaining prolonged effectiveness in complex biological environments. By comparing our polymer membrane with other recently reported oil–water separation membranes, as summarized in Table 1, it is evident that our membrane offers distinct advantages. Under comparable separation efficiencies, it demonstrates superior functionality due to its dual responsiveness to both pH and ultraviolet (UV) light. Notably, the UV-responsive behaviour is environmentally friendly and easy to implement, underscoring the enhanced performance and practical applicability of this smart polymer membrane in dynamic and complex separation environments.

Table 1 Performance comparison of oil-water separation membranes reported in recent years

Modified material	Wettability conversion condition	Separation efficiency	Separation flux ($L \cdot m^{-2} \cdot h^{-1}$)	Refs.
TiO_2 and PFOA	water and ethanol washed	>99.9 %	9.17×10^3	Kong et al.[32]
TiO_2 and fluorosurfactant	ethanol	>98.0 %	5.00×10^3	Li et al.[33]
Dual stimuli-responsive polymer coatings	UV and pH	＞97.1%	1.77×10^4	This work

Overall, this work presents a promising strategy for the development of switchable, multifunctional materials for oil-water separation. By integrating stimuli-responsive wettability, high separation efficiency (97.1%), mechanical robustness (stable over 10 photoswitchable cycles), and effective antibacterial properties (with a maximum bacterial inhibition rate of 75.1%), this coating demonstrates strong potential for practical deployment in diverse environmental and industrial scenarios, particularly in challenging oil-contaminated

settings.

CRediT authorship contribution statement

Haoqian Wang: Writing – original draft, Data curation, Funding acquisition. **Ke Wang:** Writing –review& editing. **Jiajun Zuo:** Formal analysis. **Zhihang Wang:** Conceptualization, Writing –review& editing, Investigation. **Nong Wang:** Methodology, Supervision, Software, Project administration, Funding acquisition, Resources, Writing–review& editing.

Corresponding Authors

Zhihang Wang – School of Engineering, College of Science and Engineering, University of Derby, Markeaton Street, Derby DE2 23AW, United Kingdom; orcid.org/0000-0002-9961-3346; E-mail: z.wang@derby.ac.uk; – Department of Materials Science and Metallurgy, the University of Cambridge, 27 Charles Babbage Rd, Cambridge, CB3 0FS, UK.

Nong Wang – School of Chemistry and Chemical Engineering, Lanzhou Jiaotong University, Lanzhou 730070, P. R. China. orcid.org/0000-0001-7499-0009; E-mail: wangnong07@163.com

Authors

Haoqian Wang – School of Chemistry and Chemical Engineering, Lanzhou Jiaotong University, Lanzhou 730070, P. R. China.

Ke Wang – School of Chemistry and Chemical Engineering, Lanzhou Jiaotong University, Lanzhou 730070, P. R. China.

Jiajun Zuo – School of Chemistry and Chemical Engineering, Lanzhou Jiaotong University,

Lanzhou 730070, P. R. China.

Declaration of competing interest

The authors declare no competing financial interest.

Acknowledgments

This work was supported by the Gansu Province Key Research and Development Program (Grant 23YFGA0044) and the Gansu Provincial Department of Education: Excellent Graduate Student "Innovation Star" project (Grant 2025CXZX-692).

References

[1] S. Wang, L. Yang, G. He, B. Shi, Y. Li, H. Wu, R. Zhang, S. Nunes and Z. Jiang,Two-dimensional nanochannel membranes for molecular and ionic separations.Chemical Society Reviews. 2020, 49, 1071-1089.
[2] Y. Wu and B. M. Weckhuysen,Separation and Purification of Hydrocarbons with Porous Materials.Angewandte Chemie International Edition. 2021, 60, 18930-18949.
[3] H. Wang, M. Wang, X. Liang, J. Yuan, H. Yang, S. Wang, Y. Ren, H. Wu, F. Pan and Z. Jiang,Organic molecular sieve membranes for chemical separations.Chemical Society Reviews. 2021, 50, 5468-5516.
[4] H. J. Tanudjaja, C. A. Hejase, V. V. Tarabara, A. G. Fane and J. W. Chew,Membrane-based separation for oily wastewater: A practical perspective.Water Research. 2019, 156, 347-365.
[5] C. Y. Chuah, K. Goh, Y. Yang, H. Gong, W. Li, H. E. Karahan, M. D. Guiver, R. Wang and T.-H. Bae,Harnessing Filler Materials for Enhancing Biogas Separation Membranes.Chemical Reviews. 2018, 118, 8655-8769.
[6] Q. Zhang, W. Chen, J. Zuo, G. Liu, X. Han and N. Wang,Fish Scale-Inspired β-Cyclodextrin Cross-Linked Polyacrylamide Hydrogels for Oil–Water Separation.ACS Applied Materials & Interfaces. 2025, 17, 17389-17397.
[7] C. Li, W. Wei, L. He, X. Qi, J. He, X. Zhang, X. Han, J. Wang and Z. Gao,Super-hydrophobic Fe/TiO2 membrane prepared by dynamic etching of ferric salt (II) for efficient oil-water separation and photocatalytic removal of oil pollution.Journal of Water Process Engineering. 2024, 65,
[8] Y. Zhang, A. Yi, Y. Ren, Q. Chen, J. Jiang, H. Sun, Z. Zhu and A. Li,CMPs membranes prepared using electrostatic spinning as a template for efficient oil-water separation.Journal of Environmental Chemical Engineering. 2024, 12,
[9] Z. Wu, J. Xue, J. Zhang, M. Wang, Z. Chen, Y. Lv and S. Ma,Photocatalytic self-cleaning membrane with polyaniline/NH2-MIL-125 heterojunction for highly oil-water/seawater separation and bacterial inactivation.Separation and Purification Technology. 2023, 323,

[10] Q. Sun, J. Du, L. Wang, A. Yao, Z. Song, L. Liu, D. Cao, J. Ma, W. Lim, W. He, et al.,Smart superwetting COF membrane for controllable oil/water separation.Separation and Purification Technology. 2023, 317,
[11] I. S. Al-Husaini, A. R. M. Yusoff and M. D. H. Wirzal,Efficient oil/water separation using superhydrophilic polyethersulfone electrospun nanofibrous ultrafiltration membranes.Journal of Environmental Chemical Engineering. 2022, 10,
[12] G. Parisi, P. K. Szewczyk, S. Narayan and U. Stachewicz,Photoresponsive Electrospun Fiber Meshes with Switchable Wettability for Effective Fog Water Harvesting in Variable Humidity Conditions.ACS Applied Materials & Interfaces. 2023, 15, 40001-40010.
[13] H. Liu, J. Xie, J. Zhao, R. Wang, Y. Qi and S. Sun,Temperature and photo sensitive PVDF-g-PNIPAAm/BN@PDA-Ag nanocomposite membranes with superior wasterwater separation and light-cleaning capabilities.Separation and Purification Technology. 2024, 331,
[14] H. Wang, Z. Zhang, Z. Wang, Y. Liang, Z. Cui, J. Zhao, X. Li and L. Ren,Multistimuli-Responsive Microstructured Superamphiphobic Surfaces with Large-Range, Reversible Switchable Wettability for Oil.ACS Applied Materials & Interfaces. 2019, 11, 28478-28486.
[15] J. Xie, J. Zhang, Y. Ma, Y. Han, J. Li and M. Zhu,Spiropyran-incorporated honeycomb porous films with reversible multistimuli-responsive properties.Journal of Materials Chemistry C. 2022, 10, 7154-7166.
[16] J. Chen, X. Chen, U. Azhar, X. Yang, C. Zhou, M. Yan, H. Li and C. Zong,Flexible and Photo-responsive superwetting surfaces based on porous materials coated with Mussel-Inspired Azo-Copolymer.Chemical Engineering Journal. 2023, 466,
[17] Y. Hou, D. Weng, Z. Zhang, Y. Yu, L. Chen and J. Wang,Near-Infrared Light Responsive Surface with Switchable Wettability in Microstructure and Surface Chemistry.Langmuir. 2023, 39, 6276-6286.
[18] H. Xue, Y. Han, G. Liu, W. Chen, Z. Wang and N. Wang,Photoresponsive surfactants for controllable and reversible emulsion systems.Colloids and Surfaces A: Physicochemical and Engineering Aspects. 2025, 705,
[19] L. U. Qiu, J. Zheng, X. Yu, X. Han and N. Wang,Hydrophobic Photoresponsive Azobenzene-Containing Materials Prepared by Click Reaction.Surface Review and Letters. 2023, 31,
[20] L. Baohe, L. Jiang, Y. Wang, C. Li, D. Yu and N. Wang,Construction and Properties of New-Type Photo-Responsive Molecular Imprinting Materials.Polymer Science, Series A. 2023, 64, 673-684.
[21] S. Sun, J. Dang, Q. Pan, C. Zhang and S. Liu,pH-Responsive Flexible Copper Electrode with Switchable Wettability for Electrocatalytic Hydrogen/Oxygen Evolution Reactions and Urea Oxidation Reaction.ACS Applied Materials & Interfaces. 2023, 15, 27357-27368.
[22] B. Tran, S. Watts, J. D. P. Valentin, N. Raßmann, G. Papastavrou, M. Ramstedt and S. Salentinig,pH‐Responsive Virus‐Based Colloidal Crystals for Advanced Material Platforms.Advanced Functional Materials. 2024, 34,
[23] Q. Zhang, H. Wang, L. Qiu, X. Han, Z. Wang and N. Wang,Synthesis and Characteristics of Smart Coating Materials for Reversible Double Stimulus-Responsive Oil–Water Separation.ACS Applied Polymer Materials. 2024, 6, 6482-6494.
[24] W. Dan and M. Tingting,Research on Solar Energy Resources in Hexi Region of Gansu Province.IOP Conference Series: Earth and Environmental Science. 2019, 330,
[25] D. R. Meena, S. R. Gadre and P. Balanarayan,PAREMD: A parallel program for the evaluation of momentum space properties of atoms and molecules.Computer Physics Communications. 2018, 224, 299-310.
[26] S. S. Khire, N. Sahu and S. R. Gadre,MTASpec software for calculating the vibrational IR and Raman spectra of large molecules at ab initio level.Computer Physics Communications. 2022, 270,
[27] C. Gonzalez and H. B. Schlegel,An improved algorithm for reaction path following.The Journal of Chemical Physics. 1989, 90, 2154-2161.

[28] S. Shruthi, M. Smahel, M. Kohout, G. Shanker and G. Hegde,Influence of linking units on the photo responsive studies of azobenzene liquid Crystals: Application in optical storage devices.Journal of Molecular Liquids. 2021, 339,
[29] A. Debuigne, C. Jérôme and C. Detrembleur,Organometallic-mediated radical polymerization of 'less activated monomers': Fundamentals, challenges and opportunities.Polymer. 2017, 115, 285-307.
[30] S. Perrier,50th Anniversary Perspective: RAFT Polymerization—A User Guide.Macromolecules. 2017, 50, 7433-7447.
[31] M. Uchiyama, K. Satoh and M. Kamigaito,Cationic RAFT and DT polymerization.Progress in Polymer Science. 2022, 124,
[32] W. Kong, F. Li, Y. Pan and X. Zhao,Hygro-responsive, Photo-decomposed Superoleophobic/Superhydrophilic Coating for On-Demand Oil–Water Separation.ACS Applied Materials & Interfaces. 2021, 13, 35142-35152.
[33] S. Fan, Z. Li, C. Fan, J. Chen, H. Huang, G. Chen, S. Liu, H. Zhou, R. Liu, Z. Feng, et al.,Fast-thermoresponsive carboxylated carbon nanotube/chitosan aerogels with switchable wettability for oil/water separation.Journal of Hazardous Materials. 2022, 433,